Accelerating peroxymonosulfate-based Fenton-like reaction *via* Mott-Schottky heterojunction

Yanqiu Zhang [a],[1], Dong Yang [b],[1], Shouchun Ma [b], Yang Yang [b], Yina Guan [a], Dongxu Wang [a], Yubo Zhao [a], Li Sheng [b],[*], Tongjie Yao [b],[*], Jie Wu [a],[*]

[a] *Key Laboratory of Functional Inorganic Material Chemistry, Ministry of Education, School of Chemistry and Materials Science, Heilongjiang University, Harbin 150080, China*
[b] *State Key Laboratory of Urban Water Resource and Environment, School of Chemistry and Chemical Engineering, Harbin Institute of Technology, Harbin 150001, China*

ARTICLE INFO

ABSTRACT

A Mott-Schottky heterojunction is reported to boost the peroxymonosulfate (PMS) activation in Fenton-like reaction through a non-radical path. The heterojunction with Co nanoparticles encapsulated by nitrogen-doped graphitized carbon (N-GC) shell was synthesized *via* pyrolysis of ZIF67 @ZIF8 and subsequent acidic treatment. Benefiting from Mott-Schottky effect, the electrons were transferred from Co nanoparticles to the N-GC shell, leading to the rearranged electron density on N-GC surface and improvement of the PMS activation. The PMS activation efficiency of heterojunction (86.0%) was much higher than the reference catalyst without Mott-Schottky effect (35.3%), and even comparable to Co^{2+} (86.2%). 85.0% of tetracycline (TC) removal efficiency was realized after only 10.0 s. Moreover, the intrinsic advantages of non-radical path were well inherited by Mott-Schottky heterojunction, including high anti-interfere property toward various anions, cations and organics, high catalytic activity in a wide pH range, low metal leaching, and high magnetic recyclability.

1. Introduction

The ever-growing production of organic chemicals have posed great threat to the clean drinking water. PMS-based Fenton-like reaction has been recognized as an effective technique for their elimination [1–4]. Generally, PMS activation is classified into the radical path and the non-radical path. In the former one, PMS are efficiently activated on transition metal surface for $SO_4^{\bullet-}$ or $^\bullet OH$ [5–7]. However, the toxic leached metal ions and environmentally susceptive radicals greatly restrict their wide application.

More recently, metal-free carbonaceous materials, such as graphene, carbon nanotubes (CNTs) and N-GC, have emerged as green alternatives for transition metals [8–10]. PMS are activated following a non-radical path on their surface, and activation efficiency is mainly determined by the surface electron distribution. Unfortunately, electrons on the sp^2 carbon network are uniform dispersion, resulting in a chemical inert surface [11,12]. To improve the surface reactivity, heteroatom dopants, surface defects and functional groups are engineered to tailor the surface electron distribution and break the chemical inertness [13–18].

However, the improvements are limited due to the intrinsic drawbacks in these techniques. For example, the amount of heteroatom dopants is usually less than 3.0 at% [19]. The defects only generate at the carbonaceous material edge, while the flat surface with plenty of reactive sites are free of defects [20]. Therefore, it is highly desirable to develop new approach to improve the surface reactivity.

Compared to the carbonaceous materials, metal nanoparticles (NPs) display relatively lower flat band potential [21]. After contact, carbonaceous materials functioned as the electron acceptor will continuously attract electrons from metal surface until their Fermi levels reach the same level, and this is famous for Mott-Schottky effect [22]. Some studies have already certified the positive influence of Mott-Schottky effect on accelerating reaction rate either theoretically or experimentally [21,23,24].

In this work, a Mott-Schottky heterojunction was constructed to prompt the PMS activation, where Co NPs were encapsulated inside the N-GC shell. Electrons flew from Co NPs to the N-GC shell, leading to their accumulation and re-distribution on the N-GC surface. N atoms and C atoms with inhomogeneous electron density favored for the

---

* Corresponding authors.
  E-mail addresses: shengli@hit.edu.cn (L. Sheng), yaotj@hit.edu.cn (T. Yao), wujie@hlju.edu.cn (J. Wu).
[1] These authors contributed equally to this work.

complexation with PMS, thereby PMS activation is largely improved, and the activation efficiency was even comparable to that of Co^{2+}. Moreover, Mott-Schottky heterojunction presented outstanding degradation efficiency in a wide pH range and high environmental adaption toward various cations, anions and organics. This work contributed to the first mechanistic insight into the Mott-Schottky effect in PMS-based Fenton-like reaction, and it opens up a new way for PMS efficient activation on a heterogeneous catalyst surface.

2. Material and methods

2.1. Materials

$Co(NO_3)_2 \cdot 6\ H_2O$, $Zn(NO_3)_2 \cdot 6\ H_2O$, H_2SO_4, NaOH, NaN_3, NaCl, $NaNO_3$, Na_2SO_4, Na_2CO_3, NaH_2PO_4, K_2SO_4, $CaCl_2$, $MgSO_4$, PMS, 2-methylimidazole (2-MeIM), methanol (MeOH), ethanol (EtOH), *tert*-butylalcohol (TBA), humic acid (HA), TC, rhodamine B (RhB), methyl blue (MB), methyl orange (MO), bisphenol A (BPA), p-chlorophenol (4-CP), chlortetracycline (CTC), oxytetracycline (OTC), ciprofloxacin (CIP), sulfamethoxazole (SMZ), 5,5-Dimethyl-1-pyrroline N-oxide (DMPO), nitro blue tetrazolium (NBT), 2,2,6,6-tetramethyl-4-piperidino (TEMP), and 2,2,6,6-tetramethylpiperidine 1-oxyl (TEMPO) were purchased from China Pharmaceutical Chemical Reagent Co., Ltd. All chemicals were analytical grade and used as received. The deionized water was purified through a Millipore system with a resistivity of 18.2 $M\Omega \cdot cm^{-1}$.

2.2. Synthesis of ZIF67 @ZIF8

ZIF67 @ZIF8 was prepared according to the previous reports with minor modifications [25]. Firstly, 1.09 g of $Co(NO_3)_2 \cdot 6\ H_2O$, 2.22 g of $Zn(NO_3)_2 \cdot 6\ H_2O$ and 2.46 g of 2-MeIM were respectively dispersed into 15.0, 13.0 and 30.0 mL of MeOH. Then, $Co(NO_3)_2 \cdot 6\ H_2O$ solution was mixed with 2-MeIM solution. After stirring for 5.0 min, $Zn(NO_3)_2 \cdot 6\ H_2O$ solution was injected into the above mixture, and the reaction was performed at room temperature for 4.0 h. The products were centrifuged and washed with MeOH for 3.0 times, and finally dried at 60 °C overnight.

2.3. Synthesis of P-ZIF67 @ZIF8, EP-ZIF67 @ZIF8, EP-ZIF67 and EP-ZIF8

ZIF67 @ZIF8 powders were heated in a tube furnace at 800 °C for 2.0 h under N_2 atmosphere with a heating rate of 2.0 °C/min, and the products were assigned as P-ZIF67 @ZIF8. 100 mg of P-ZIF67 @ZIF8 powders were added into 3.0 M of H_2SO_4 solution. After standing for 5.0 h, the products were washed by deionized water until the solution pH≈ 7.0, and EP-ZIF67 @ZIF8 were prepared. The recipe for EP-ZIF67 or EP-ZIF8 were similar to that of EP-ZIF67 @ZIF8, except ZIF67 @ZIF8 were replace by ZIF67 or ZIF8 (Text. S1).

2.4. Fenton-like reaction

Typically, 4.0 mg of catalysts were added into 50 mL of TC solution (20 mg/L) under magnetic stirring for 10.0 min to reach adsorption-desorption equilibrium. Subsequently, 4.0 mg of PMS were added into the above solution to initiate the Fenton-like reaction. At the given time interval, 3.0 mL of the solution was sampled and filtered through a filter membrane with a pore size of 0.45 μm to remove the catalysts. The filtrate was immediately measured by UV-Vis spectrophotometry (Labtech UV9100B) to determine the concentration of residual TC solution. The pH was adjusted by H_2SO_4 or NaOH solution, and the standard Fenton-like reaction was carried out at pH= 7.0.

After the Fenton-like reaction, the solid catalysts were removed through filter membrane with pore size of 0.45 μm. Then, the PMS and TC were re-added into the filtrate to initiate the homogeneous Fenton-like reaction by leached metal ions.

2.5. Characterization

The crystalline phases of the catalysts were characterized by X-ray diffraction (XRD) using a Smartlab apparatus ($Cu_{K\alpha}$ radiation, $\lambda = 1.5418$ Å, $2\theta = 5-80°$). The morphology and microstructure were characterized by scanning electron microscope (SEM, Hitachi S4800), transmission electron microscope (TEM, JEOL JEM-2100), high-resolution TEM (HRTEM), high-angle annular dark-field scanning TEM (HAADF-STEM) and elemental mappings. X-ray photoelectron spectrum (XPS) was measured on an ULTRA AXIS DLD X-ray photoelectron spectrometer with $Al_{K\alpha}$ excitation. Electron paramagnetic resonance (EPR) spectroscopy was applied for radical measurement (Bruker A200 spectrometer). The detailed information was given in the supporting information (Text S2). Brunauer-Emmett-Teller (BET) specific surface area was obtained by measuring N_2 adsorption-desorption with a Beckman Coulter 3100 pore size and surface area analyzer. The degradation intermediates of TC were identified by high performance liquid chromatography coupled to micro TOF-Q II time-of-flight mass spectrometry (HPLC-MS, Agilent 1260 HPLC/Bruker micro TOF-Q II). Inductively coupled plasma atomic spectroscopy (ICP) was performed on an Optima 7000 DV. The mineralization of TC was tested by a total organic carbon analyzer (TOC-VCPH/CPN, Shimadzu, Japan). Scanning Kelvin probe (SKP) measurement was performed under ambient condition (SKP5050 system, Scotland). Linear sweep voltammetry (LSV) and chronoamperometry test (i-t curve) were conducted on a CHI 760E electrochemical system (Shanghai, China). The zeta-potential was measured using a Malvern ZS90 zeta-potential analyzer. The Computation method was described in Text S3.

3. Results and discussion

3.1. Synthesis and characterization

The synthetic strategy of EP-ZIF67 @ZIF8 is shown in Fig. 1. Firstly, ZIF67 @ZIF8 were prepared and served as templates. During calcination at 800 °C under N_2 atmosphere, the coordination bonds between organic linkers and metal nodes in both ZIF67 and ZIF8 were broken [26]. Co nodes in ZIF67 were aggregated into Co NPs, while Zn nodes in ZIF8 were sublimated due to the low boiling point at nanosized level [27]. Meanwhile, 2-MeIM were carbonized to N-GC, and the dodecahedral morphology of template was preserved.

As shown in Fig. S1, ZIF67 @ZIF8 templates present the rhombic dodecahedral morphology with an average size of 430 nm. TEM image shows a solid structure, nevertheless, the core@shell structure cannot be distinguished due to the similar brightness contrast between ZIF67 and ZIF8. The dispersions of elements Zn and Co are analyzed by elemental mapping, where the element Co are concentrated in the core position, while the element Zn are mainly distributed in the shell region. After overlapping, ZIF67 is fully covered by ZIF8, indicating a well-defined
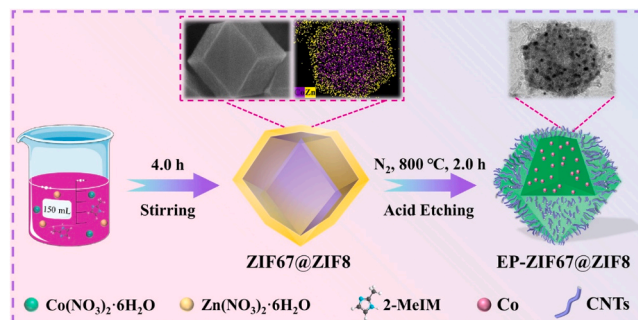

Fig. 1. Synthesis process of EP-ZIF67 @ZIF8.

core@shell structure.

After pyrolysis (Fig. S2), the dodecahedral morphology of P-ZIF67 @ZIF8 is observed, while the size is reduced from 430 to 330 nm. Numerous nanosized Co NPs are randomly distributed, whose average size is about 60 nm. Plenty of CNTs grew on the P-ZIF67 @ZIF8 surface, and the hollow channel is witnessed by the corresponding TEM images.

After H_2SO_4 etching (Figs. 2a-c), EP-ZIF67 @ZIF8 presents the similar shape as P-ZIF67 @ZIF8. Some Co NPs are survival owing to the seamlessly wrapped by N-GC shell, however, the amount remarkably reduces and the diameter decreases to 16 nm. Numerous CNTs still exist on the EP-ZIF67 @ZIF8 surface, and entangle with each other (Fig. 2d). (111) crystal plane of Co NPs and (002) crystal plane of N-GC shell are observed, whose lattice spacing is 0.21 and 0.35 nm, respectively (Fig. 2e) [28]. The signal of element Co is scattered, corresponding to the dispersed Co NPs. The signal of element Zn is diluted, owing to sublimation under the high-temperature (Figs. 2f and 2g). N_2 adsorption-desorption isotherm of EP-ZIF67 @ZIF8 with surface area of 584.7 m^2/g presents a type-IV isotherm model (Fig. S3a). A significant hysteresis loops appeared at high pressure ($P/P_0 > 0.45$) indicate the existence of mesopores, and the pore diameters are mainly concentrated at 8.9 and 24.2 nm (Fig. S3b) [29].

The formation mechanism of CNTs is investigated. CNTs are invisible on P-ZIF8 surface, suggesting the catalytic effect of Co NPs plays a crucial role in their formation (Fig. S4) [27]. After pyrolysis of ZIF67 (Fig. S5), the dodecahedral shape cannot maintain, revealing the protective function of ZIF8 shell in preservation of integrated dodecahedral structure. Only a small amount of CNTs are observed due to lack of carbon species, indicating ZIF8 shell are served as the extra carbon source for CNT growth. After soaking in H_2SO_4 solution, majority of Co NPs are etched, except those deeply encapsulated by N-GC shell

(Fig. S6). The morphology of EP-ZIF8 is not obviously changed in comparison with P-ZIF8 (Fig. S7).

In XRD patterns, diffraction peaks of ZIF67, ZIF8 and ZIF67 @ZIF8 are the same, and match well with the simulated standard card (Fig. S8a) [30]. A broad peak centered at 26.2° is visible in EP-ZIF8, corresponding to (002) plane of N-GC (Fig. S8b) [28]. A peak assigned to (111) plane of Co NPs appears at 44.3° in EP-ZIF67. For EP-ZIF67 @ZIF8, three sharp peaks at 44.3, 51.5 and 75.9° are corresponding to (111), (200) and (220) planes of Co NPs (JCPDS NO. 15–0806) [31]. High intensity reflects the high content. During the pyrolysis of ZIF67 @ZIF8, ZIF8 shell was served as extra carbon source, and more wrapped Co NPs were avoided to be etched.

Surface compositions of catalysts were tested by XPS measurement. The survey XPS spectra confirmed the existence of elements C, N, O, Co and Zn in EP-ZIF67 @ZIF8, while only C, N, O and Zn were present in EP-ZIF8 (Figs. S9a and S9b). Fig. S9c shows the high-resolution N 1 s spectrum of EP-ZIF67 @ZIF8, four peaks are corresponding to the oxidized-N (403.4 eV), graphitic-N (400.9 eV), pyrrolic-N (399.8 eV) and pyridinic-N (398.4 eV), respectively [32]. The core-level spectrum of EP-ZIF8 exhibits the similar conformations of doped N atoms (Fig. S9d). According to the previous study, graphitic-N atoms can attract electron from neighboring C atoms, resulting in the positively charged C atoms and negatively charged N atoms [33–35]. C-N bonds appeared in EP-ZIF67 @ZIF8 and EP-ZIF8 favor the electron transfer (285.7 eV in Figs. S9e and S9f) [35]. Other two peaks in core-level C 1 s spectra with binding energies of 289.3 and 284.6 eV are correlated with the oxidized-C and C-C/C=C bond [35]. As revealed in Fig. S9g, XPS spectrum of Co $2p_{3/2}$ could be deconvoluted into three peaks, corresponding to metallic Co (778.1 eV) and N-coordinated Co^{2+}/Co^{3+} (779.4/781.6 eV), respectively [22,29]. The signal of Co 2p is clearly
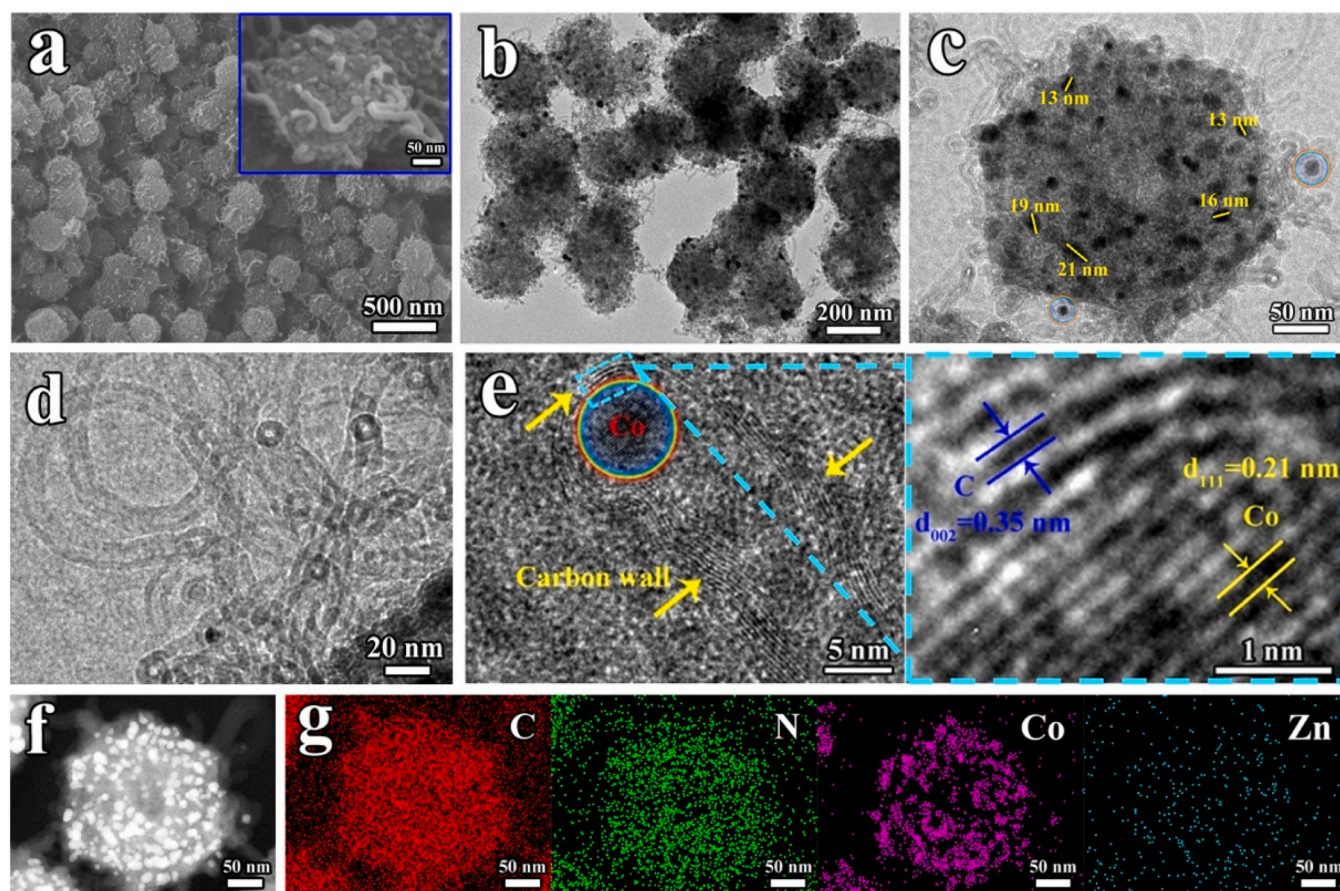

Fig. 2. Morphological and structural information of the EP-ZIF67 @ZIF8: (a) SEM image; (b-d) TEM images; (e) HRTEM images; (f) HAADF-STEM image; (g) elemental mappings. Inset shows the corresponding magnified image.

observable, while that of Zn 2p is weak, further confirming the existence of Co NPs and removal of element Zn in EP-ZIF67 @ZIF8 (Figs. S9g and S9h).

3.2. Degradation performance

TC were employed as the targeted pollutants to assess the performance of various catalysts in PMS-based Fenton-like reaction. Catalysts and TC were added into solution and stirred for 30 min, the solution was sampled every 10 min for UV–vis analysis. In Fig. S10a, after 10.0 min, the adsorption-desorption equilibrium was realized. As shown in Fig. 3a, only 5.0% of TC are removed after 10.0 min by individual PMS, indicting the low self-activation efficiency and the necessity of catalysts. The adsorption efficiencies at 10.0 min are 22.5%, 22.3% and 35.6% for EP-ZIF8, EP-ZIF67 and EP-ZIF67 @ZIF8, respectively. After adding PMS into EP-ZIF67 @ZIF8 solution, TC are rapidly decomposed, and the degradation efficiency is as high as 85.0% within 10.0 s, and the value further increases to 94.7% after 10.0 min. For comparison, the degradation efficiencies of EP-ZIF8 and EP-ZIF67 are 27.8% and 56.2% at 10.0 s, and 47.9% and 87.7% at 10.0 min. These results indicate EP-ZIF67 @ZIF8 presents the best catalytic activity. Table S1 lists some works on Fenton-like reaction towards TC degradation, in which the EP-ZIF67 @ZIF8 can be comparable to other catalysts.

Heterogeneous Fenton-like reaction was accompanied with the homogeneous Fenton-like reaction, which was initiated by leaching ions from catalyst surface. In Fig. 3b, the degradation efficiency contributed by homogeneous reaction of EP-ZIF67 @ZIF8, EP-ZIF67 and EP-ZIF8 are only 1.8%, 6.3% and 0.3%, respectively, suggesting most of TC are removed by heterogeneous Fenton-like reaction. ICP data indicate the leached Co^{2+} from EP-ZIF67 @ZIF8 (0.280 mg/L) is 11 times lower than that from EP-ZIF67 (3.060 mg/L), due to the thicker N-GC shell covered on the Co NP surface. In addition, the leached Zn^{2+} from EP-ZIF67 @ZIF8 and EP-ZIF8 are 0.061 mg/L and 0.105 mg/L, respectively.

EP-ZIF67 @ZIF8 presented high degradation performance and low metal leaching, and their work condition was further optimized. As shown in Fig. S10b, the degradation efficiencies at 10.0 min prompt from 80.7% to 95.3% by increasing the catalyst dosage from 1.0 to 10 mg. When the PMS dosages are in the range of 1.0–4.0 mg, the degradation efficiencies monotonously increase from 83.5% to 94.7%. Further increasing to 10 mg, the efficiency is almost unchanged (94.4%) in Fig. S10c.

The influence of solution pH values on TC degradation is shown in Fig. 3c. More than 86.0% of TC degradation efficiency is realized in a wide range (pH=1.0–9.0), indicating EP-ZIF67 @ZIF8 show excellent activity under acidic, neutral and weakly basic conditions. However, TC
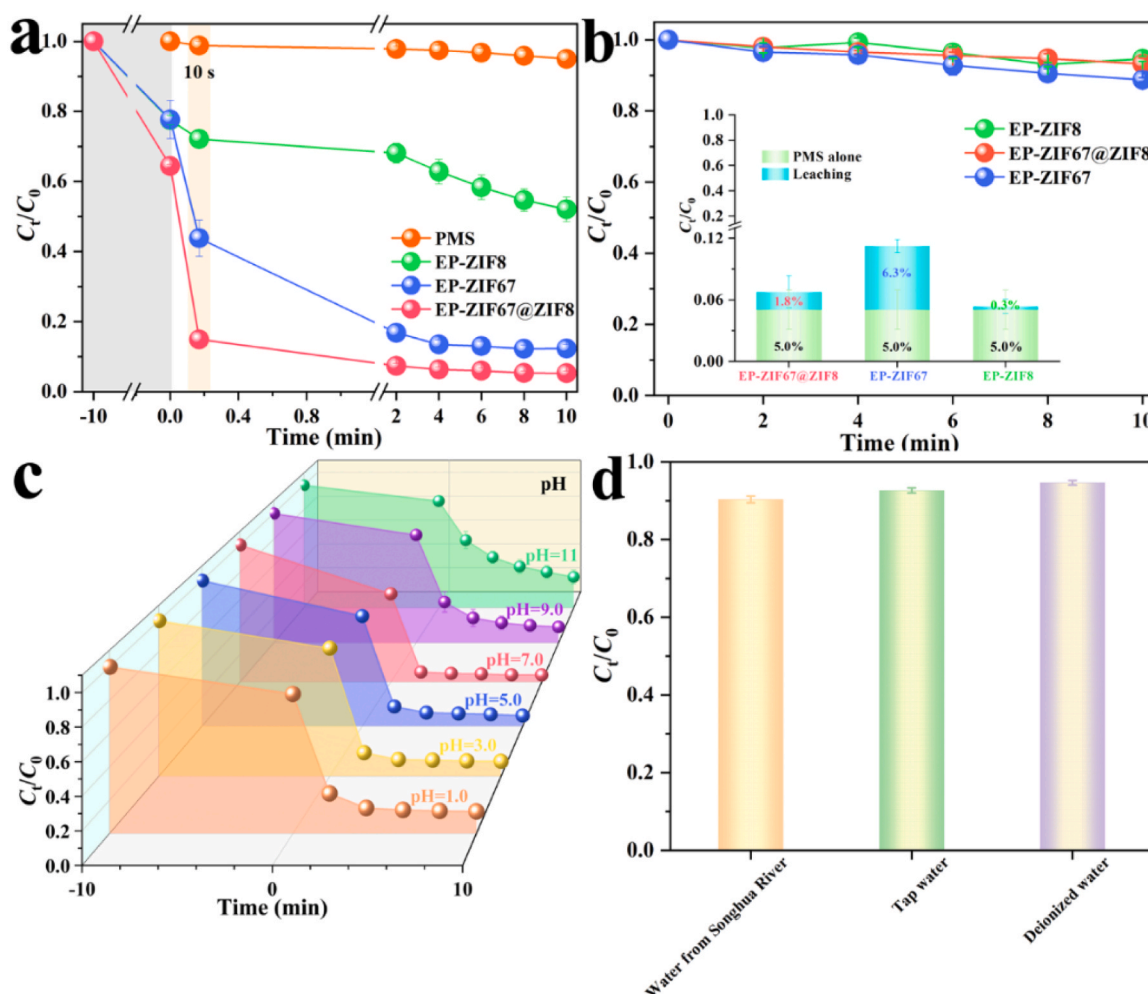

Fig. 3. (a) TC degradation in the presence of various catalysts, negative time represents the adsorption time in darkness. (b) TC degradation in homogeneous Fenton-like reaction. Inset shows PMS self-activation efficiencies without catalysts (green column), and contributions from homogeneous reaction catalyzed by various catalysts+PMS systems (blue column). Influence parameters on degradation process: (c) solution pH values; (d) solution prepared by *Songhua River* water and tap water. Reaction conditions for Fig. 3a: catalyst= 4.0 mg, [TC]= 20 mg/L and PMS= 4.0 mg. For Fig. 3b: PMS= 4.0 mg, [TC]= 20 mg/L and the solvents were the filtrates after Fenton-like reaction catalyzed by the corresponding catalysts.

removal efficiency decreases to 74.7% at pH= 11.0, since PMS is likely to hydrolyze to SO_5^{2-} under the basic condition, whose oxidative capacity is much lower than that of $SO_4^{\bullet-}$ [36–38]. To better explain the influence of solution pH values on degradation process, zeta potentials on catalyst surface under different pH values were investigated in Fig. S10d. Under the acidic and neutral condition (pH=1.0–7.0), the catalyst surface are positively charged. Previous studies reported that TC mainly existed in the form of TCH_3^+ at pH< 3.3 [39]. Therefore, the electrostatic repulsion between the catalyst surface and TCH_3^+ inhibited the adsorption and degradation of TC at pH= 1.0–3.0. The TC molecule mainly presented as TCH_2^0 under 3.30 <pH< 7.68. In this case, the electrostatic force between the catalyst surface and TC molecules was canceled, and the degradation rate was maximized. The isoelectric point (pH_{PZC}) on catalyst surface is 8.5, and the catalyst surface is negatively charged in alkaline environment (Fig. S10d). TC mainly existed as TCH^- under 7.68 <pH< 9.70 and TC^{2-} under pH> 9.70. From the viewpoint of electrostatic force, it was easy to explain why the degradation rate was reduced in the solution with the pH = 9.0 and 11. In fact, the pH values of actual wastewater are usually in range of 5.0–9.0, meaning the EP-ZIF67 @ZIF8 are valuable in real application [40]. For verification, TC solutions are prepared by *Songhua River* water and tap water. In Fig. 3d, TC degradation process is almost unaffected, and at least 90.0% of TC is removed after 10.0 min in these two cases. According to above

analysis, 4.0 mg of catalysts, 4.0 mg of PMS, and solution pH= 7.0 were selected as the standard condition in the following experiments.

The degradation paths of TC were analyzed. Based on density functional theory (DFT) calculation, the frontier molecular orbitals of TC were gained by employing Gaussian 09 software. According to the Highest Occupied Molecular Orbital (HOMO) and Lowest Unoccupied Molecular Orbital (LUMO) in Fig. 4a and b, the HOMO of TC is predominately localized on benzene ring (R1), carbon-carbon double bond (S4) and hydroxyl groups (S1, S2 and S3), indicating these sites are more likely to be attacked and oxidized (Fig. 4c). The possible intermediates generated in TC degradation process were analyzed by HPLC-MS (Fig. 4d-f) [41]. Three routines were proposed, which was consistent with DFT analysis. In routine-I, because R1 and S1 sites are oxidized in the Fenton-like reaction, P1 ($m/z = 483$) is obtained *via* ring-opening reaction [42]. In routine-II, after the S2 site is attacked, initial TC transforms to P2 ($m/z = 428$) *via* dehydroxylation. In routine-III, the destruction of S3 and S4 sites results in the formation of P3 ($m/z = 461$) by hydroxylation. After further dehydroxylation, deamination, and dealkylation, these intermediates are decomposed to P4, P5, and P6 with $m/z = 459$, 442, and 369. Finally, ring-opening intermediates with low molecule weight are obtained, such as P7 ($m/z = 355$), P8 ($m/z = 295$), P9 ($m/z = 279$) and P10 ($m/z = 281$), which are eventually mineralized to CO_2 and H_2O. The mineralization performance was tested by TOC
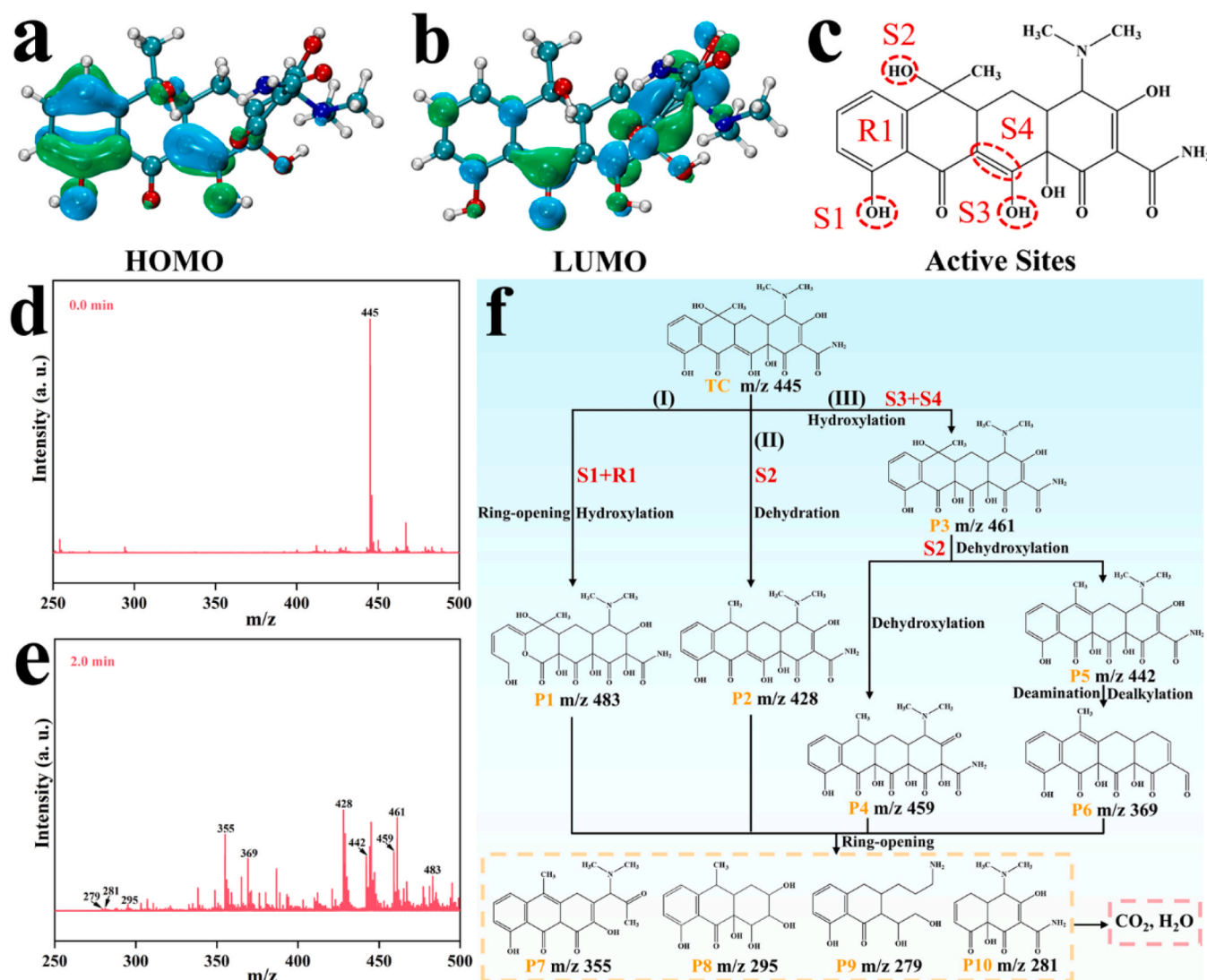

Fig. 4. (a, b) HOMO and LUMO of TC molecule; (c) active sites on TC molecule. HPLC-MS spectra of TC degradation at (d) 0.0 min and (e) 2.0 min. (f) Possible TC degradation routines. Reaction condition at ambient temperature: EP-ZIF67 @ZIF8 = 4.0 mg, [TC]= 20 mg/L and PMS= 4.0 mg.

measurement, and the value is as high as 46.4%, indicating that most of TC and intermediates are mineralized at 10.0 min

The acute toxicity, developmental toxicity and mutagenicity of TC as well as its degradation intermediates were assessed by quantitative structure-activity relationship (QSAR) prediction using Toxicity Estimation Software Tool (T.E.S.T.) model software (version 5.1). The acute toxicities were evaluated by two different levels: the LC_{50} of fathead minnow (the concentration of a chemical that causes 50% fathead minnow to die after 96 h), the LC_{50} of daphnia magna (the concentration

of a chemical that causes 50% of daphnia magna to die after 48 h). Notably, the LC_{50} values of fathead minnow and daphnia magna for most of the degradation intermediates are higher than initial TC (Figs. S11a and S11b), suggesting that a large number of intermediates are less toxic than TC [43]. Furthermore, the developmental toxicity is evaluated in Fig. S11c. Three intermediates (P3, P8 and P9) are lower "developmental toxicant" than TC, and the intermediates of P1 is even "developmental non-toxicant". The mutagenicity information provided in Fig. S11d shows that P9 is "mutagenicity negative", and P1 and P5
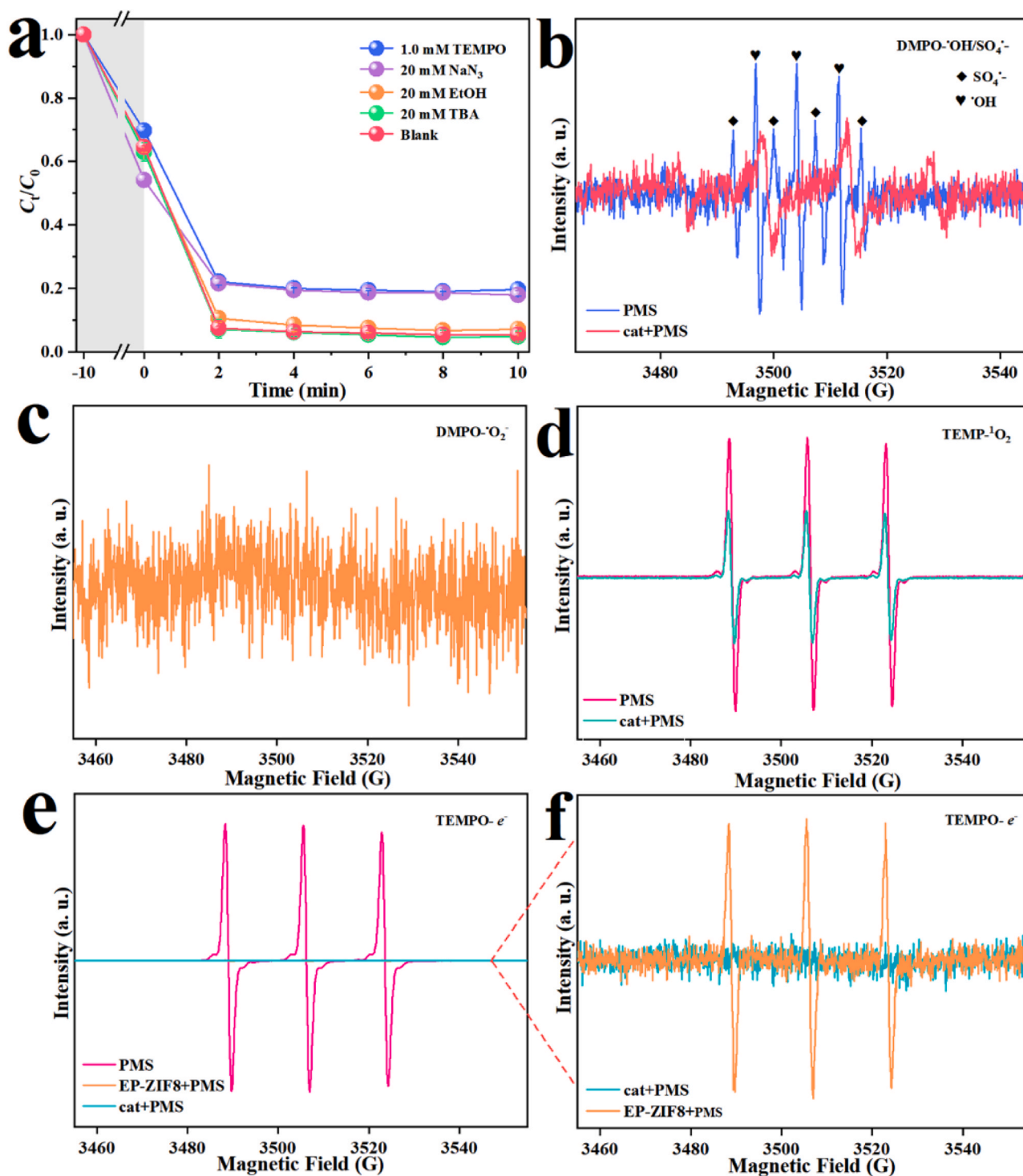

Fig. 5. (a) Radical trapping experiments in the presence of different scavengers. EPR spectra of various catalysts+PMS systems: (b) DMPO-$^{\bullet}$OH/SO$_4^{\bullet-}$; (c) DMPO-$^{\bullet}$O$_2^-$; (d) TEMP-^{1}O$_2$; (e) TEMPO-e^- and (f) corresponding magnified image of Fig. 5e. "cat" represents EP-ZIF67 @ZIF8.

have much lower mutagenicity compared to TC. Thus, it could be concluded that TC was oxidized into compounds with low toxicity.

3.3. Identification of ROSs

3.3.1. $SO_4^{\bullet-}$ and $\bullet OH$

Reactive oxygen species (ROSs) involved into Fenton-like reaction are explored *via* trapping experiments. Generally, EtOH was used as scavenger of both $SO_4^{\bullet-}$ and $^\bullet OH$ ($SO_4^{\bullet-}/^\bullet OH$), while TBA was only susceptive to $^\bullet OH$ [44]. In Fig. 5a, the retarding effect of EtOH and TBA on degradation efficiency is negligible, implying the scarce yields of $SO_4^{\bullet-}/^\bullet OH$. This is further confirmed by EPR analysis using DMPO as trapping reagent (Fig. 5b). In the presence of individual PMS, seven characteristic peaks assigned to $SO_4^{\bullet-}/^\bullet OH$ with intensity ratio of 1:2:1:2:1:2:1 are observed [40]. Nevertheless, the signal disappears in EP-ZIF67 @ZIF8 +PMS system.

$SO_4^{\bullet-}/^\bullet OH$ are the main radicals generated during PMS activation on transition metal surface. Their absence in EPR analysis indicates PMS are not activated on Co NP surface (Eqs. 1 and 2) [45]. Co NPs could survive after soaking in 3.0 M of H_2SO_4 solution for 5.0 h, suggesting N-GC shell were served as barriers between wrapped Co NPs and external solution. Therefore, the contact between Co NPs and PMS was unavailable.

$$\equiv Co(II) + HSO_5^- \rightarrow \equiv Co(III) + SO_4^{\bullet-} + OH^- \qquad (1)$$

$$\equiv Co(II) + HSO_5^- \rightarrow \equiv Co(III) + HSO_4^- + \bullet OH \qquad (2)$$

3.3.2. $\bullet O_2^-$ and $^1O_2$

Signal of DMPO-$^\bullet O_2^-$ is invisible in Fig. 5c, indicating little amount of $^\bullet O_2^-$ is produced in EP-ZIF67 @ZIF8 +PMS system. NBT was employed as a characteristic molecule probe for $^\bullet O_2^-$ due to formation of mono-formazan, whose absorption peak was at 530 nm in UV-Vis spectrum [28]. In Fig. S12, the absorption peak of monoformazan is invisible, confirming the scarce $^\bullet O_2^-$ yield. Moreover, in trapping experiment, the retarding effect of TEMPO (scavenger of $^\bullet O_2^-$) in TC degradation is limited, further confirming the minor role of $^\bullet O_2^-$ (Fig. 5a) [46].

The contribution of $^1O_2$ is investigated using NaN_3 as scavenger [46], and the degradation efficiency only reduces from 94.7% (blank solution) to 82.1%, indicating $^1O_2$ are not the main active species (Fig. 5a). For further verification, EPR experiment was carried out using TEMP as trapping reagent in Fig. 5d [47]. The signal intensity of TEMP-$^1O_2$ in EP-ZIF67 @ZIF8 +PMS system is even lower than that in the individual PMS system, suggesting the lowered $^1O_2$ yield after adding EP-ZIF67 @ZIF8.

3.3.3. Electron

As depicted in Fig. 5e and f, the signal intensities of TEMPO-e^- in EP-ZIF67 @ZIF8 +PMS system and EP-ZIF8 +PMS system are significantly reduced, in comparison with that in the individual PMS system, demonstrating a large number of electrons are produced in Fenton-like reaction [25]. EP-ZIF67 @ZIF8 +PMS system yields the maximum amount of electrons due to the lowest signal intensity. Based on above analysis, we could conclude that electrons played the dominating role among various ROSs.

3.4. Catalytic mechanism

In comparison with EP-ZIF8, EP-ZIF67 @ZIF8 displayed much better degradation performance. Therefore, some questions were raised: Did Co NPs really unavailable for TC degradation? If not, how did they participate into the Fenton-like reaction? Herein, the catalytic mechanism in EP-ZIF67 @ZIF8 +PMS system toward TC degradation was investigated.

3.4.1. Mott-Schottky effect

The work function of Co NPs and N-GC are tested by SKP analysis, and the values are 5.19 and 5.33 eV, respectively (Fig. 6a). After contact, electrons inevitably transfer from Co NPs to N-GC shell, and accumulate on the N-GC side until their Fermi levels are equal, owing to the Mott-Schottky effect [23]. According to XPS analysis, graphitic-N atoms attracted electrons from neighboring C atoms through C-N bonds, leading to the positively charged C atoms (Figs. S9e and S9f). In this case, the negatively charged PMS is likely to adsorb on the C atom sites *via* coulomb interaction.

DFT calculations were employed for insights into the Mott-Schottky effect. Herein, N-GC/Co model and N-GC model are used for describing EP-ZIF67 @ZIF8 and EP-ZIF8, and they are respectively displayed in Figs. S13 and S14. Firstly, the electron transfer and rearranged electron density on N-GC layer were analyzed. In N-GC/Co model, the distance between N-GC layer and adjacent Co layer is 2.181 Å. According to the charge analysis, electrons easily transfer from Co layer to N-GC layer due to the different work functions, leading to their accumulation on the N-GC layer (Table S2). In N-GC/Co model and N-GC model, three C atoms around the graphitic-N atom are denoted as C1, C2 and C3, respectively (Figs. 6b and c). Graphitic-N atom can attract electrons from C1, C2 and C3 atoms, due to the higher electronegativity. As shown in Table S3, graphitic-N atoms are negatively charged, and C1, C2 and C3 atoms are positively charged. Nevertheless, in comparison with N-GC model, C1, C2 and C3 atoms in N-GC/Co model possess less positive charge due to the accumulation of electrons on N-GC layer (Fig. 6b and 6c).

3.4.2. Formation of PMS-catalyst complex

After adding PMS into EP-ZIF67 @ZIF8 solution, the current output immediately ascends, and quickly reaches a platform, suggesting the electron migration between PMS and catalyst for the formation of "PMS-catalyst complex" (Fig. 6d) [44]. For comparison, the increase amplitude is small after adding EP-ZIF8, due to the lack of Mott-Schottky effect. This was consistent with the EPR analysis that more electrons are produced on the EP-ZIF67 @ZIF8 surface (Fig. 5f).

The formation process of PMS-catalyst complex is simulated in Figs. 7 and 8. In light of chemical environment, O atoms in PMS molecule are classified into three types: O1, O2 and O3 (Fig. 7), and they are preferred to bind with C1 atom with more positive charge (Table S3, Figs. 6b and c). The type-I, type-II and type-III represent the corresponding PMS adsorption structures, and the optimized configurations are shown in Fig. 7 and Fig. S15. In Table S4, adsorption energy (E_{ads}) between PMS configurations and underlying catalysts are calculated. All E_{ads} values are negative, reflecting the exothermic adsorption process and stable adsorption structures. It is worth noting that the adsorption capacity of N-GC/Co for PMS is higher than that of N-GC, suggesting N-GC/Co is functioned as a better substrate for PMS molecule. The charge density difference reveals the electrons transfer from N-GC/Co and N-GC to the PMS after adsorption, which elongates the O-O bond in PMS molecule (Fig. 8). Compared to N-GC+PMS, the amount of transferred charge in N-GC/Co+PMS system is higher, indicating PMS are preferred to be activated on N-GC/Co surface for PMS-catalyst complex.

3.4.3. Activation of PMS and degradation of TC

After adding TC into EP-ZIF67 @ZIF8 +PMS system (Fig. 6d), the current output sharply rises, due to electron extraction from TC to PMS-catalyst complex [28]. Then, the value quickly decreases owing to the PMS-catalyst complex activation and TC degradation, and this also reflects the oxidative potential of PMS-catalyst complex is higher than that of TC. For comparison, the increase amplitude of current output in EP-ZIF8 +PMS system is much smaller, suggesting the limited transferred electron amount. The sluggish current decrease reflects the slow TC degradation rate. Besides i-t curve, LSV curve also presents the similar result during the PMS-catalyst complex formation and activation processes. Namely, the current output ascends step by step after adding PMS and TC in sequence (Fig. 9a) [48]. The electron migration between
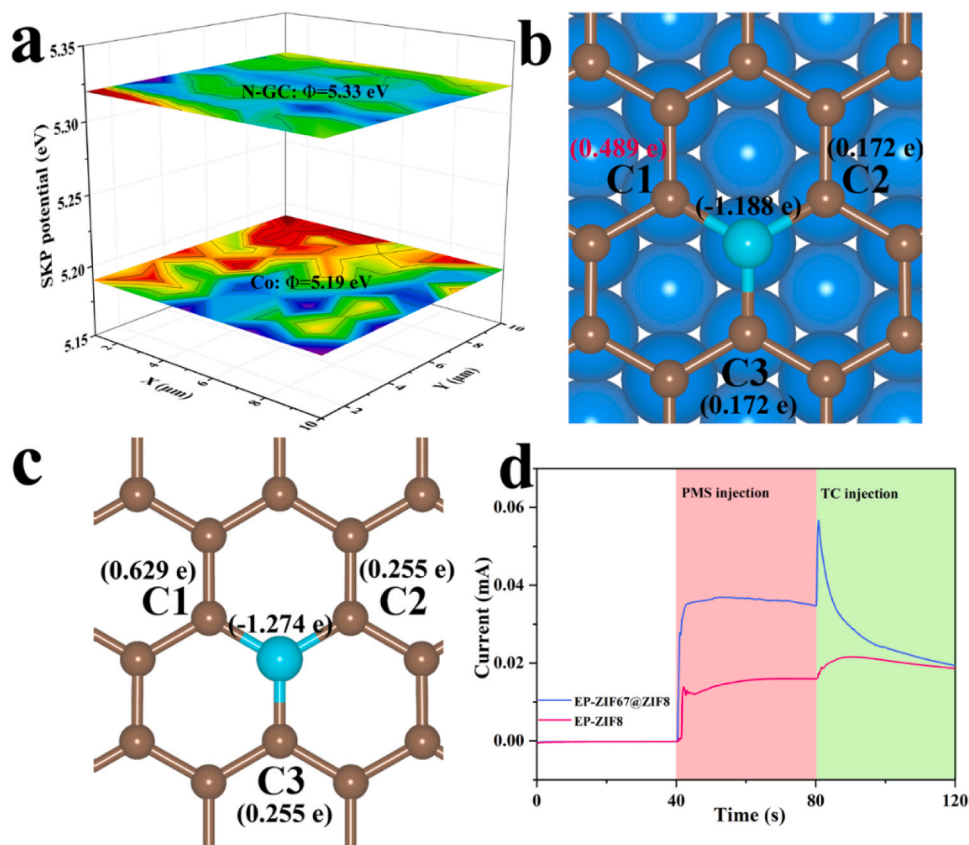
Fig. 6. (a) SKP maps of N-GC layer and Co NPs. Local structure near the graphitic-N atom: (b) N-GC/Co model and (c) N-GC model. (d) The i-t curves for electron transfer path after adding PMS and TC step by step.
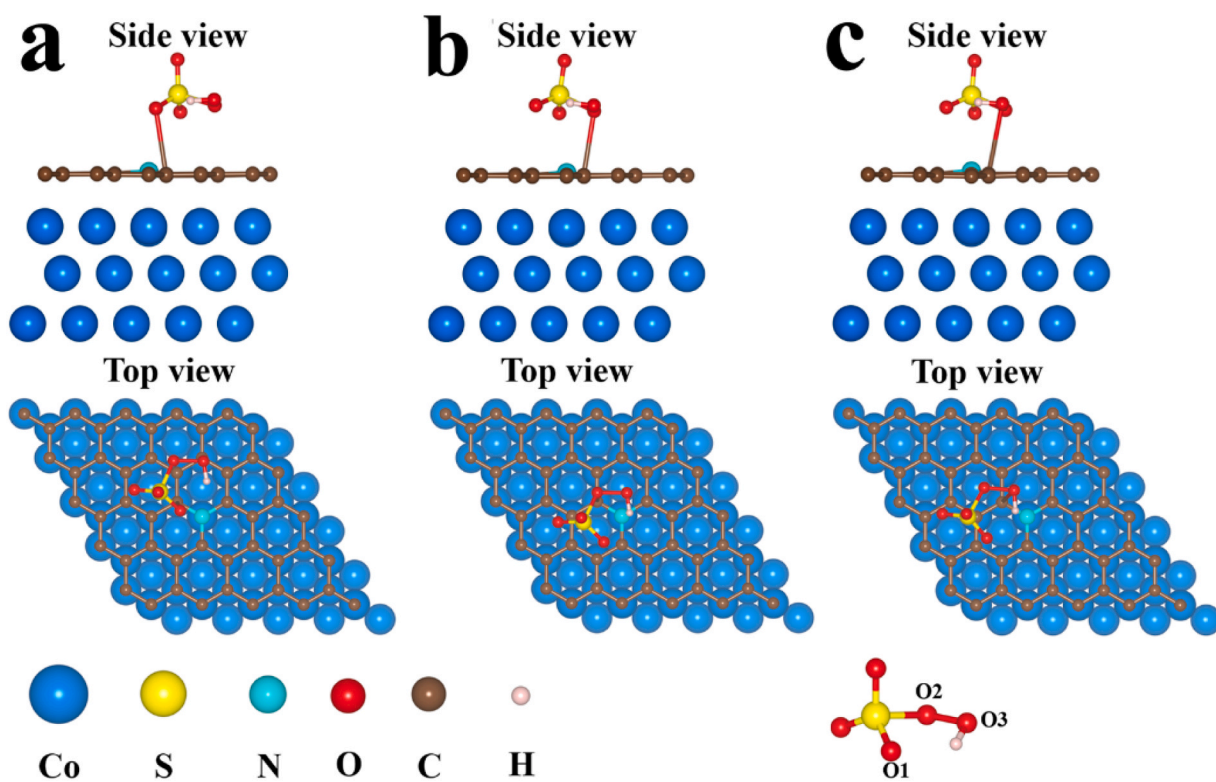

Fig. 7. Adsorption configurations of PMS molecule adsorbed on the N-GC/Co surface: (a) type-I; (b) type-II and (c) type-III adsorption.
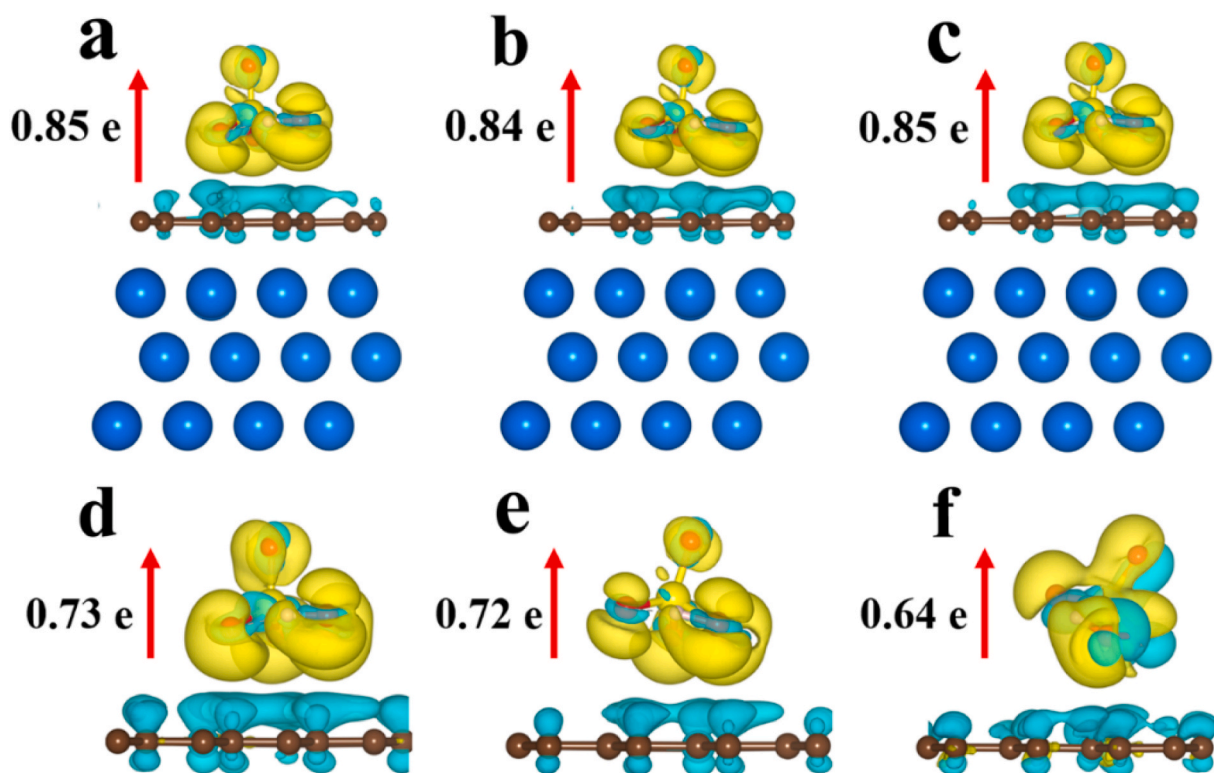
Fig. 8. Charge density difference of (a) type-I; (b) type-II and (c) type-III adsorption in N-GC/Co+PMS system; (d) type-I; (e) type-II and (f) type-III adsorption in N-GC+PMS system. Yellow region and cyan region respectively represent the charge accumulation and charge depletion.
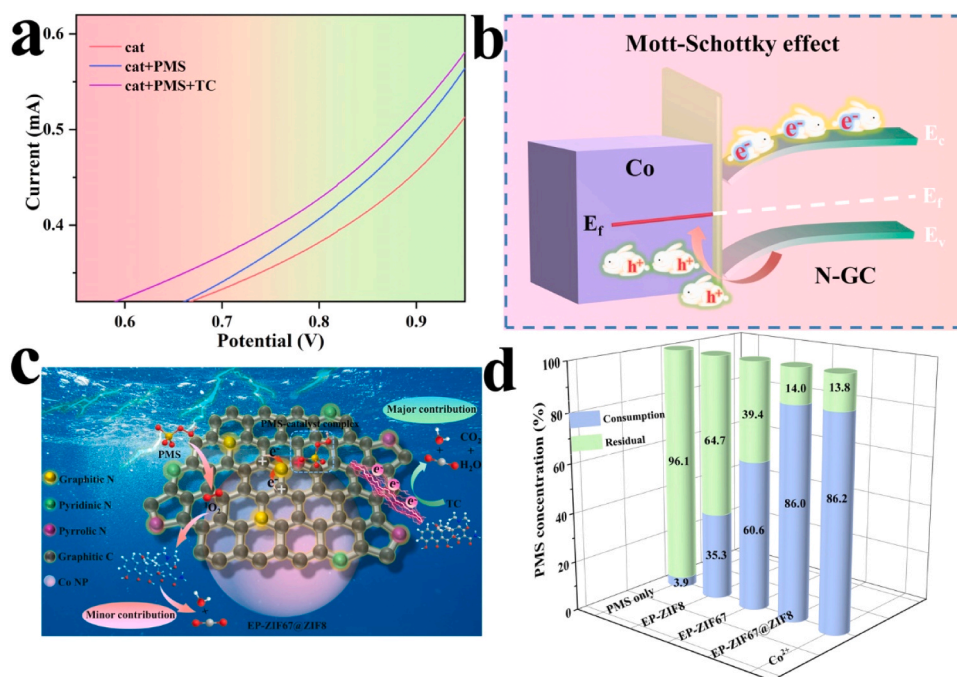

Fig. 9. Electrochemical test for electron transfer path: (a) LSV curves for EP-ZIF67 @ZIF8, where "cat" represents EP-ZIF67 @ZIF8. Schematic illustration of (b) Mott-Schottky effect and (c) degradation mechanism on EP-ZIF67 @ZIF8 surface. (d) PMS utilization efficiency and residual efficiency in various catalysts+PMS systems.
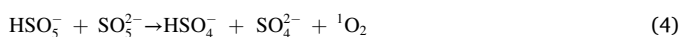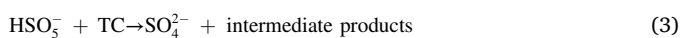
TC molecule and PMS-catalyst complex is simulated. The work function (Φ) is defined as the difference between the Fermi energy (E_f) and vacuum energy (E_{vac}). As shown in Table S5, the Φ of N-GC/Co is 5.176 eV. After adsorption with PMS, the value of PMS-catalyst complex significantly increases to about 6.80 eV, meaning PMS-catalyst complex

easily attract electrons from TC *via* mediated-electron-transfer mechanism, comparing to the original N-GC/Co substrate.

3.4.4. Possible catalytic mechanism and high PMS activation efficiency
Based on above results, a possible catalytic mechanism on EP-

ZIF67 @ZIF8 surface is proposed, where PMS activation is divided into three steps: (i) the deeply encapsulated Co NPs were incapable for PMS activation *via* Eqs. 1 and 2. Instead, electrons on Co NP surface transferred to N-GC surface due to the Mott-Schottky effect (Fig. 9b). (ii) Benefiting from the accumulated electrons on N-GC surface, the electron distribution was rearranged, leading to PMS-catalyst complex formation (Fig. 9c). (iii) After interaction with TC, the electrons immediately transferred from TC molecule to PMS-catalyst complex, resulting in activation of PMS-catalyst complex and degradation of TC (Eqs. 3 and 4) [44,49].

$$HSO_5^- + TC \rightarrow SO_4^{2-} + \text{intermediate products} \tag{3}$$

$$HSO_5^- + SO_5^{2-} \rightarrow HSO_4^- + SO_4^{2-} + {}^1O_2 \tag{4}$$

In EP-ZIF67 @ZIF8, Mott-Schottky effect is crucial for enhanced PMS activation efficiency. For verification, the activation efficiency is calculated in Fig. 9d (Text S4) [20]. PMS self-activation efficiency is only 3.9%, and this well explains their inferior degradation performance (Fig. 3a). In EP-ZIF8 +PMS system, the PMS activation efficiency is improved to 35.3%. For comparison, the activation efficiency of EP-ZIF67 @ZIF8 +PMS system is as high as 86.0%, and the value is even comparable to that of Co^{2+} (86.2%), which is recognized as the most effective homogeneous catalyst for PMS activation. Furthermore, the activation efficiencies of EP-ZIF67 +PMS system (60.6%) lies between EP-ZIF8 and EP-ZIF67 @ZIF8, since the amount of encapsulated Co NPs is smaller than that in EP-ZIF67 @ZIF8.

3.5. Versatility and recyclability

One of the outstanding advantages for PMS activation *via* non-radical path is the excellent environmental adaptation. In Fig. 10a, the degradation performance is little affected in the presence of 10 mM of

common inorganic anions, including CO_3^{2-}, SO_4^{2-}, Cl^-, $H_2PO_4^-$ and NO_3^-. Na^+, Ca^{2+}, Mg^{2+} and K^+ also display minor retarding effect toward the degradation efficiency (Fig. 10b). Although TC removal efficiencies are reduced due to the occupation of the active sites by HA molecules in the range of 0.5–10 mg/L, 83.2% of TC is still degraded within 10.0 min in the presence of 10 mg/L of HA (Fig. S16).

The versatility of EP-ZIF67 @ZIF8 is measured by degrading 10 organic pollutants (Fig. 10c). At least 90.0% of removal efficiencies are realized at 10.0 min for common phenols (20 mg/L of BPA and 20 mg/L of 4-CP), cationic dyes (20 mg/L of MO and 20 mg/L of RhB), anionic dyes (5 mg/L of MB), antibiotics (20 mg/L of TC, 20 mg/L of CTC and 20 mg/L of OTC) and fluoroquinolone (5 mg/L of CIP). Although the degradation efficiency of sulfonamide (10 mg/L of SMZ) is somewhat low, 81.2% of efficiency is still achieved.

Another advantage of EP-ZIF67 @ZIF8 is the rapid magnetic separation from the aqueous solution (Fig. S17). Their stability and reusability are also vital in practical wastewater treatment. In Fig. 10d, after 5 successive cycles, 87.4% of degradation efficiency of the 1st cycle is still maintained. Furthermore, TEM image, SEM image and XRD pattern of the recycled catalysts show the structure and crystalline are little changed (Figs. S18 and S19). Co NPs are still seamlessly confined inside the N-GC shell after Fenton-like reaction (Fig. S18b), which is another evidence for the impossible contact between Co NPs and external solution.

4. Conclusion

In this work, the EP-ZIF67 @ZIF8 Mott-Schottky heterojunctions were prepared, and used as catalysts in PMS-based Fenton-like reaction. TC removal efficiency is as high as 85.0% at 10.0 s, superior than that of EP-ZIF8 without Mott-Schottky effect (27.8%). Among various ROSs, electrons were responsible for TC removal, suggesting PMS activation on
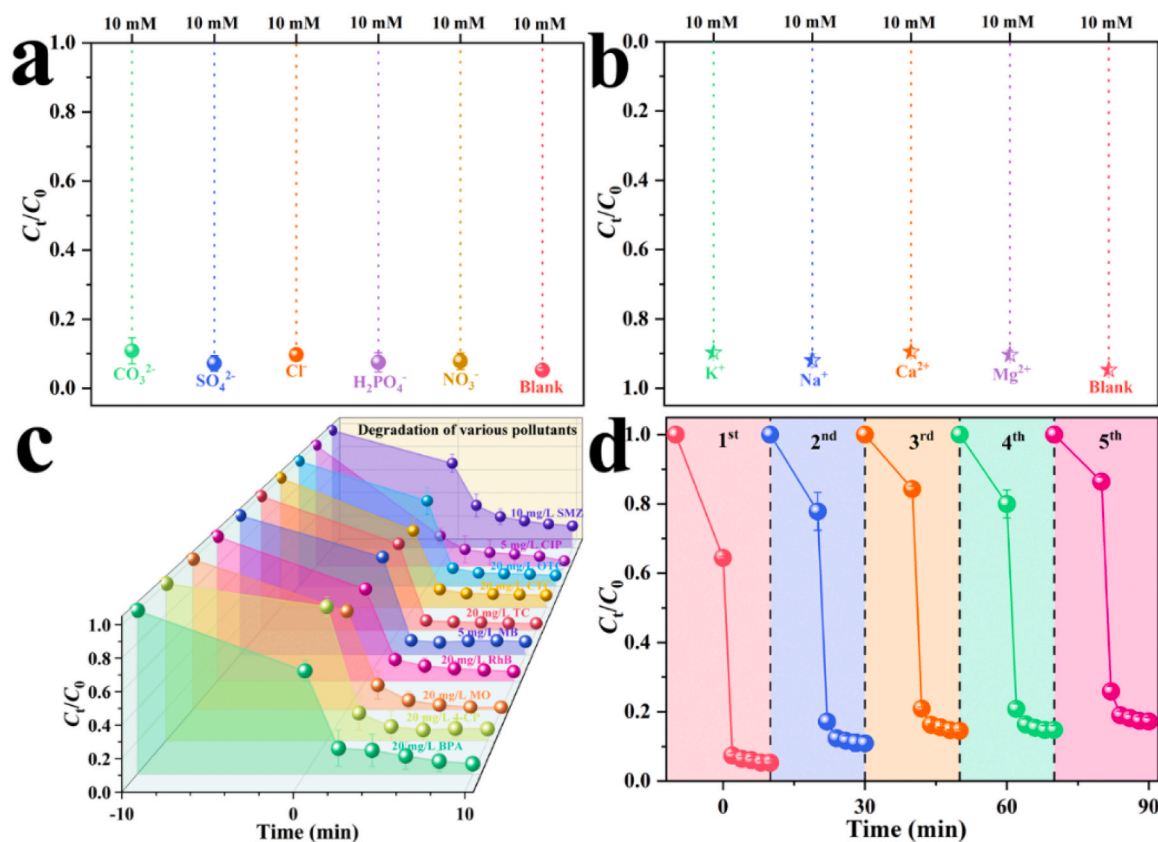

Fig. 10. Influence of (a) various anions; (b) cations on degradation process. (c) Degradation processes toward various pollutants. (d) Recycled experiments in 5 successive runs.

N-GC surface followed the non-radical path. Theoretical simulation and experiment data indicated that electrons flew from Co NPs to N-GCs due to the Mott-Schottky effect, leading to the re-distribution of electron density on N-GC surface. As a result, PMS activation efficiency on EP-ZIF67 @ZIF8 surface (86.0%) is much higher than that on EP-ZIF8 surface (35.2%), and even comparable to Co^{2+} ions (86.2%). Besides high degradation rate, Mott-Schottky heterojunctions also showed good anti-interference property toward various anions, cations and natural organics. 87.4% of degradation efficiency of the 1st cycle was maintained after the 5th cycle. EP-ZIF67 @ZIF8 with high activation efficiency, good environmental adaptability, low leaching and excellent stability could be used as promising catalysts in environmental remediation.

CRediT authorship contribution statement

Yanqiu Zhang: Formal analysis, Investigation, Data curation, Writing – original draft, Writing – review & editing. **Dong Yang:** Validation, Investigation, Software. **Shouchun Ma:** Validation, Investigation. **Yang Yang:** Writing – review & editing. **Yina Guan:** Methodology. **Dongxu Wang:** Formal analysis. **Yubo Zhao:** Formal analysis. **Li Sheng:** Conceptualization, Supervision. **Tongjie Yao:** Conceptualization, Writing – review & editing, Funding acquisition. **Jie Wu:** Conceptualization, Supervision, Project administration, Funding acquisition.

Declaration of Competing Interest

The authors declare that they have no known competing financial interests or personal relationships that could have appeared to influence the work reported in this paper.

Data Availability

Data will be made available on request.

Acknowledgments

Appendix A. Supporting information

Supplementary data associated with this article can be found in the online version at doi:10.1016/j.apcatb.2023.123059.

References

[1] Z. Wu, Y. Wang, Z. Xiong, Z. Ao, S. Pu, G. Yao, B. Lai, Core-shell magnetic Fe_3O_4@ Zn/Co-ZIFs to activate peroxymonosulfate for highly efficient degradation of carbamazepine, Appl. Catal. B: Environ. 277 (2020), 119136.

[2] X. Duan, J. Kang, W. Tian, H. Zhang, S.-H. Ho, Y.-A. Zhu, Z. Ao, H. Sun, S. Wang, Interfacial-engineered cobalt@carbon hybrids for synergistically boosted evolution of sulfate radicals toward green oxidation, Appl. Catal. B: Environ. 256 (2019), 117795.

[3] H. Zhu, A. Guo, S. Wang, Y. Long, G. Fan, X. Yu, Efficient tetracycline degradation *via* peroxymonosulfate activation by magnetic Co/N co-doped biochar: Emphasizing the important role of biochar graphitization, Chem. Eng. J. 450 (2022), 138428.

[4] E.-T. Yun, G.-H. Moon, H. Lee, T.H. Jeon, C. Lee, W. Choi, J. Lee, Oxidation of organic pollutants by peroxymonosulfate activated with low-temperature-modified nanodiamonds: understanding the reaction kinetics and mechanism, Appl. Catal. B: Environ. 237 (2018) 432–441.

[5] F. Wang, H. Fu, F.-X. Wang, X.-W. Zhang, P. Wang, C. Zhao, C.-C. Wang, Enhanced catalytic sulfamethoxazole degradation *via* peroxymonosulfate activation over amorphous CoS_x@SiO_2 nanocages derived from ZIF-67, J. Hazard. Mater. 423 (2022), 126998.

[6] A. Wang, Z. Zheng, H. Wang, Y. Chen, C. Luo, D. Liang, B. Hu, R. Qiu, K. Yan, 3D hierarchical H_2-reduced Mn-doped CeO_2 microflowers assembled from nanotubes

[7] as a high-performance Fenton-like photocatalyst for tetracycline antibiotics degradation, Appl. Catal. B: Environ. 277 (2020), 119171.

[7] C. Wang, J. Kim, M. Kim, H. Lim, M. Zhang, J. You, J.-H. Yun, Y. Bando, J. Li, Y. Yamauchi, Nanoarchitectured metal-organic framework-derived hollow carbon nanofiber filters for advanced oxidation processes, J. Mater. Chem. A 7 (2019) 13743–13750.

[8] H. Zhang, L. Lyu, Q. Fang, C. Hu, S. Zhan, T. Li, Cation-π structure inducing efficient peroxymonosulfate activation for pollutant degradation over atomically dispersed cobalt bonding graphene-like nanospheres, Appl. Catal. B: Environ. 286 (2021), 119912.

[9] H. Dai, W. Zhou, W. Wang, Z. Liu, Unveiling the role of cobalt species in the Co/N-C catalysts-induced peroxymonosulfate activation process, J. Hazard. Mater. 426 (2022), 127784.

[10] Y. Jiang, J. Zhang, R. Balasubramanian, Nitrogen-doped graphene aerogels with rational indium hydroxide decoration for highly efficient photocatalytic of p-nitrophenol, J. Environ. Chem. Eng. 10 (2022), 107125.

[11] S. Liu, Q.X. Pan, J. Li, M. Wang, J. Zhang, Y.Q. Song, C. Zhao, J. Shi, H.P. Deng, Enhanced mediated electron transfer pathway of peroxymonosulfate activation dominated with graphitic-N for the efficient degradation of various organic contaminants in multiple solutions, ACS ES&T, Water 2 (2022) 817–829.

[12] Y. Liu, W. Miao, X. Fang, Y. Tang, D. Wu, S. Mao, MOF-derived metal-free N-doped porous carbon mediated peroxydisulfate activation *via* radical and non-radical pathways: Role of graphitic N and C-O, Chem. Eng. J. 380 (2020), 122584.

[13] Y. Zhang, Y. Sun, Y. Man, H. Yuan, R. Zhao, G. Xiang, X. Jiang, L. He, S. Zhang, Highly efficient adsorption and catalytic degradation of aflatoxin B_1 by a novel porous carbon material derived from Fe-doped ZIF-8, Chem. Eng. J. (2022), 135723.

[14] X. Rong, H.J. Wang, X.L. Lu, R. Si, T.B. Lu, Controlled synthesis of a vacancy-defect single-atom catalyst for boosting CO_2 electroreduction, Angew. Chem. Int. Ed. 59 (2020) 1961–1965.

[15] X. Wang, J. Li, Q. Xue, X. Han, C. Xing, Z. Liang, P. Guardia, Y. Zuo, R. Du, L. Balcells, J. Arbiol, J. Llorca, X. Qi, A. Cabot, Sulfate-decorated amorphous-crystalline cobalt-iron oxide nanosheets to enhance O-O coupling in the oxygen evolution reaction, ACS Nano 17 (2023) 825–836.

[16] X.P. Yin, H.J. Wang, S.F. Tang, X.L. Lu, M. Shu, R. Si, T.B. Lu, Engineering the coordination environment of single-atom platinum anchored on graphdiyne for optimizing electrocatalytic hydrogen evolution, Angew. Chem. Int. Ed. 57 (2018) 9382–9386.

[17] J. Ji, Q. Yan, P. Yin, S. Mine, M. Matsuoka, M. Xing, Tuning redox reactions *via* defects on $CoS_{2−x}$ for sustainable degradation of organic pollutants, Angew. Chem. Int. Ed. 60 (2021) 2903–2908.

[18] Y. Yang, J. Mao, D. Yin, T. Zhang, C. Liu, W. Hao, Y. Wang, J. Hao, Synergy of S-vacancy and heterostructure in $BiOCl/Bi_2S_{3−x}$ boosting room-temperature NO_2 sensing, J. Hazard. Mater. 455 (2023), 131591.

[19] H. Fan, H. Yu, Y. Zhang, Y. Zheng, Y. Luo, Z. Dai, B. Li, Y. Zong, Q. Yan, Fe-doped Ni_3C nanodots in N-soped carbon nanosheets for efficient hydrogen-evolution and oxygen-evolution electrocatalysis, Angew. Chem. Int. Ed. 56 (2017) 12566–12570.

[20] C. Fu, G. Sun, G. Yin, C. Wang, G. Ran, Q. Song, P/N co-doped carbon sheet for peroxymonosulfate activation: Edge sites enhanced adsorption and subsequent electron transfer, Sep. Purif. Technol. 292 (2022), 120922.

[21] H. Su, K.X. Zhang, B. Zhang, H.H. Wang, Q.Y. Yu, X.H. Li, M. Antonietti, J.S. Chen, Activating cobalt nanoparticles *via* the Mott-Schottky effect in nitrogen-rich carbon shells for base-free aerobic oxidation of alcohols to esters, J. Am. Chem. Soc. 139 (2017) 811–818.

[22] Y. Li, W. Wang, B. Zhang, L. Fu, M. Wan, G. Li, Z. Cai, S. Tu, X. Duan, Z.W. Seh, J. Jiang, Y. Sun, Manipulating redox kinetics of sulfur species using Mott-Schottky electrocatalysts for advanced lithium-sulfur batteries, Nano Lett. 21 (2021) 6656–6663.

[23] H. Chen, K. Shen, Q. Mao, J. Chen, Y. Li, Nanoreactor of MOF-derived yolk-shell Co@C-N: Precisely controllable structure and enhanced catalytic activity, ACS Catal. 8 (2018) 1417–1426.

[24] Z.L. Wang, X.F. Hao, Z. Jiang, X.P. Sun, D. Xu, J. Wang, H.X. Zhong, F.L. Meng, X. B. Zhang, C and N hybrid coordination derived Co-C-N complex as a highly efficient electrocatalyst for hydrogen evolution reaction, J. Am. Chem. Soc. 137 (2015) 15070–15073.

[25] S. Ma, D. Yang, Y. Guan, Y. Yang, Y. Zhu, Y. Zhang, J. Wu, L. Sheng, L. Liu, T. Yao, Maximally exploiting active sites on yolk@shell nanoreactor: Nearly 100% PMS activation efficiency and outstanding performance over full pH range in Fenton-like reaction, Appl. Catal. B: Environ. 316 (2022) 121594.

[26] H.R. Chen, K. Shen, J.Y. Chen, X.D. Chen, Y.W. Li, Hollow-ZIF-templated formation of a ZnO@C-N-Co core-shell nanostructure for highly efficient pollutant photodegradation, J. Mater. Chem. A 5 (2017) 9937–9945.

[27] W. Shao, C. He, M. Zhou, C. Yang, Y. Gao, S. Li, L. Ma, L. Qiu, C. Cheng, C. Zhao, Core-shell-structured MOF-derived 2D hierarchical nanocatalysts with enhanced Fenton-like activities, J. Mater. Chem. A 8 (2020) 3168–3179.

[28] C. Zhu, Y. Nie, S. Zhao, Z. Fan, F. Liu, A. Li, Constructing surface micro-electric fields on hollow single-atom cobalt catalyst for ultrafast and anti-interference advanced oxidation, Appl. Catal. B: Environ. 305 (2022), 121057.

[29] H. Dai, W. Zhou, W. Wang, Co/N co-doped carbonaceous polyhedron as efficient peroxymonosulfate activator for degradation of organic pollutants: Role of cobalt, Chem. Eng. J. 417 (2021), 127921.

[30] Y. Zhan, S.Z. Yu, S.H. Luo, J. Feng, Q. Wang, Nitrogen-coordinated CoS_2@NC yolk-shell polyhedrons catalysts derived from a metal-organic framework for a highly reversible $Li-O_2$ battery, ACS Appl. Mater. Interfaces 13 (2021) 17658–17667.

[31] H. Chen, K. Shen, Y. Tan, Y. Li, Multishell hollow metal/nitrogen/carbon dodecahedrons with precisely controlled architectures and synergistically enhanced catalytic properties, ACS Nano 13 (2019) 7800–7810.

[32] Y. Gao, T. Li, Y. Zhu, Z. Chen, J. Liang, Q. Zeng, L. Lyu, C. Hu, Highly nitrogen-doped porous carbon transformed from graphitic carbon nitride for efficient metal-free catalysis, J. Hazard. Mater. 393 (2020), 121280.

[33] M. He, P. Zhao, R. Duan, S. Xu, G. Cheng, M. Li, S. Ma, Insights on the electron transfer pathway of phenolic pollutant degradation by endogenous N-doped carbonaceous materials and peroxymonosulfate system, J. Hazard. Mater. 424 (2022), 127568.

[34] Y. Feng, W. Sang, Z. Deng, S. Zhang, C. Li, Co-N-C@SiO$_2$ core@shell architectures enhanced stability to activate peroxymonosulfate (PMS) for efficient sulfamethoxazole degradation, Sep. Purif. Technol. 280 (2022), 119783.

[35] Y. Gao, Z. Chen, Y. Zhu, T. Li, C. Hu, New insights into the generation of singlet oxygen in the metal-free peroxymonosulfate activation process: Important role of electron-deficient carbon atoms, Environ. Sci. Technol. 54 (2020) 1232–1241.

[36] X. Li, S. Wang, P. Chen, B. Xu, X. Zhang, Y. Xu, R. Zhou, Y. Yu, H. Zheng, P. Yu, Y. Sun, ZIF-derived non-bonding Co/Zn coordinated hollow carbon nitride for enhanced removal of antibiotic contaminants by peroxymonosulfate activation: Performance and mechanism, Appl. Catal. B: Environ. 325 (2023), 122401.

[37] M. Wang, Q. Gao, M. Zhang, Y. He, Y. Zhang, R. Shen, J. Hu, G. Wu, Boosting peroxymonosulfate activation *via* highly active and durable cobalt catalysts, J. Mater. Chem. A 9 (2021) 2308–2318.

[38] H. Zeng, L. Deng, Z. Shi, J. Luo, J. Crittenden, Heterogeneous degradation of carbamazepine by Prussian blue analogues in the interlayers of layered double hydroxides: performance, mechanism and toxicity evaluation, J. Mater. Chem. A 7 (2019) 342–352.

[39] X. Deng, Y. Yang, Y. Mei, J. Li, C. Guo, T. Yao, Y. Guo, B. Xin, J. Wu, Construction of Fe3O4@FeS2@C@MoS2 Z-scheme heterojunction with sandwich-like structure: Enhanced catalytic performance in photo-Fenton reaction and mechanism insight, J. Alloy. Compd. 901 (2022), 163437.

[40] Z. Wu, Z. Xiong, R. Liu, C. He, Y. Liu, Z. Pan, G. Yao, B. Lai, Pivotal roles of N-doped carbon shell and hollow structure in nanoreactor with spatial confined Co species in peroxymonosulfate activation: Obstructing metal leaching and enhancing catalytic stability, J. Hazard. Mater. 427 (2022), 128204.

[41] Y. Yang, W. Ji, X. Li, H. Lin, H. Chen, F. Bi, Z. Zheng, J. Xu, X. Zhang, Insights into the mechanism of enhanced peroxymonosulfate degraded tetracycline using metal organic framework derived carbonyl modified carbon-coated Fe^0, J. Hazard. Mater. 424 (2022), 127640.

[42] Z.X. Wang, Y.F. Han, W.L. Fan, Y.X. Wang, L.H. Huang, Shell-core MnO$_2$/Carbon@Carbon nanotubes synthesized by a facile one-pot method for peroxymonosulfate oxidation of tetracycline, Sep. Purif. Technol. 278 (2022), 119558.

[43] Y. Yang, S. Ma, J. Qu, J. Li, Y. Liu, Q. Wang, J. Jing, Y. Yuan, T. Yao, J. Wu, Transforming type-II Fe$_2$O$_3$@polypyrrole to Z-scheme Fe$_2$O$_3$@polypyrrole/ Prussian blue *via* Prussian blue as bridge: Enhanced activity in photo-Fenton reaction and mechanism insight, J. Hazard. Mater. 405 (2021), 124668.

[44] L. Peng, Y. Shang, B. Gao, X. Xu, Co$_3$O$_4$ anchored in N, S heteroatom co-doped porous carbons for degradation of organic contaminant: role of pyridinic N-Co binding and high tolerance of chloride, Appl. Catal. B: Environ. 282 (2021), 119484.

[45] X. Li, X. Yan, X. Hu, R. Feng, M. Zhou, L. Wang, Hollow Cu-Co/N-doped carbon spheres derived from ZIFs as an efficient catalyst for peroxymonosulfate activation, Chem. Eng. J. 397 (2020), 125533.

[46] J. Li, Y. Mei, S. Ma, Q. Yang, B. Jiang, B. Xin, T. Yao, J. Wu, Internal-electric-field induced high efficient type-I heterojunction in photocatalysis-self-Fenton reaction: Enhanced H$_2$O$_2$ yield, utilization efficiency and degradation performance, J. Colloid Interf, Sci 608 (2022) 2075–2087.

[47] L.-S. Zhang, X.-H. Jiang, Z.-A. Zhong, L. Tian, Q. Sun, Y.-T. Cui, X. Lu, J.-P. Zou, S.-L. Luo, Carbon nitride supported high-loading Fe single-atom catalyst for activation of peroxymonosulfate to generate ^{1}O$_2$ with 100% selectivity, Angew. Chem. Int. Ed. 60 (2021) 21751–21755.

[48] S. Zuo, Z. Guan, D. Xia, F. Yang, H. Xu, M. Huang, D. Li, Polarized heterogeneous CuO-CN for peroxymonosulfate nonradical activation: An enhancement mechanism of mediated electron transfer, Chem. Eng. J. 420 (2021), 127619.

[49] Y. Zhao, B. Li, Y. Li, X. Fan, F. Zhang, G. Zhang, Q. Xia, W. Peng, Synergistic activation of peroxymonosulfate between Co and MnO for bisphenol A degradation with enhanced activity and stability, J. Colloid Interf. Sci. 623 (2022) 775–786.